National Oceanography Centre

NATURAL ENVIRONMENT RESEARCH COUNCIL

Coastal & Open Ocean Surface Currents Mission Study: Wavemill Product Assessment (WaPA)

Invitation to Tender AO/1-7051/12/NL/AF

WP2300 Analyses and Validation of the Wavemill airborne Proof-of-Concept data

Adrien Martin (NOC), Christine Gommenginger (NOC)

National Oceanography Centre

8th September 2014

Version 1.0

National Oceanography Centre, Southampton
European Way, Southampton
SO14 3ZH, United Kingdom
Tel: +44 (0)23 80596413 Fax: +44 (0)23 80596400

Document Signature Table

	Name	Institution	Signature	Date
Prepared by	A. Martin	NOC		01/08/2014
Revised by	C. Gommenginger	NOC		27/08/2014
Authorised by	C. Gommenginger	NOC		08/09/2014

Dissemination

Christopher Buck, ESA	Christopher.Buck@esa.int
David Cotton, SATOC Ltd	d.cotton@satoc.eu
Jose Marquez, Starlab	jose.marquez@starlab.es
Bertrand Chapron, Ifremer	Bertrand.Chapron@ifremer.fr
Geoff Burbidge, Airbus D & S	geoff.burbidge@astrium.eads.net

Issue Record

Issue n°	date	sections affected	relevant information
v1.0	08/09/2014	—	first issue

Contents

Introduction

This report presents the results of re-analyses of the airborne Wavemill Proof-of-Concept (PoC) data acquired in a star pattern over the Irish Sea in October 2011. The work was carried out in the context of WP2300 of the ESA WaPA study. The focus is mainly on the data acquired on the first day of the campaign (26/10/2011) when the Wavemill airborne demonstrator was flown in the 'Javelin' configuration [Wavemill PoC, 2012]. Some results from the data acquired on the second day (27/10/2011) in 'hybrid' configuration are presented briefly in the final section.

The report is organised as follows: first, in Section 1, the geophysical and environmental conditions observed in the area during the first flight are presented, followed in Section 2 by the description of the Wavemill PoC airborne data. In section 3, the computation of the line-of-sight and surface velocity from the SAR interferogram is described, followed by a presentation of the theoretical basis to estimate surface motion produced by waves, which is called here "wave artefact velocity". The velocity results obtained with the Wavemill PoC data are presented in Section 4.1, while Section 4.2 briefly considers possible causes for the observed spatial variability in each run. The report concludes with Section 5, including some questions and remarks about the discrepancies observed with previous analyses.
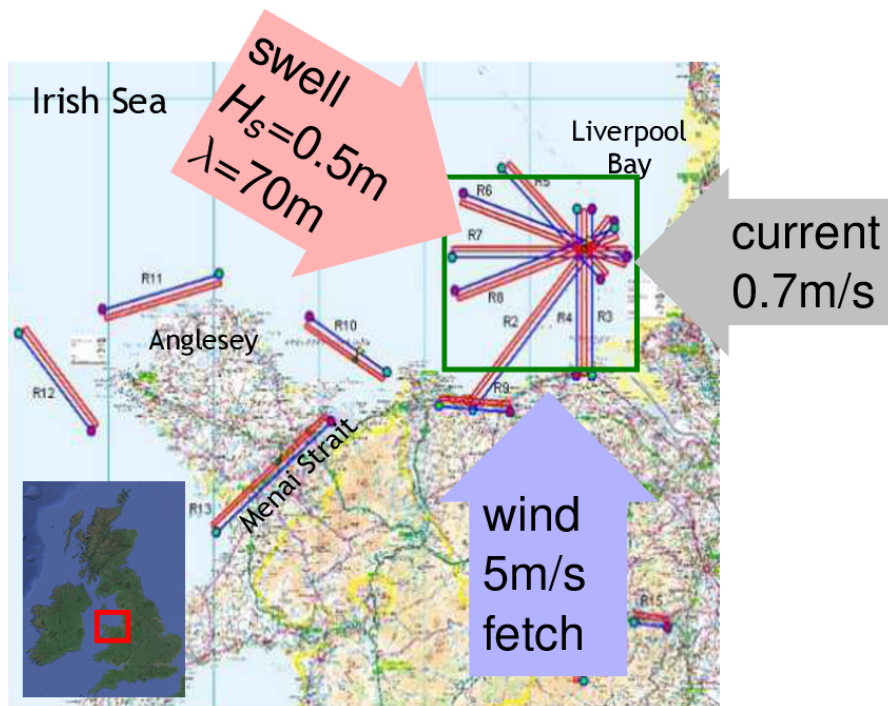
1 Geophysical Conditions

The geophysical conditions described here are for Liverpool Bay on the 26th of October 2011 between 00h and 01h30 UTC i.e. at the time of the airborne flights. These conditions were estimated thanks to various in situ observations (e.g. ADCP, HF radar, wave buoy) and atmospheric wind model output, and are summarised in Figure 1. The figure also shows the location of the various Wavemill runs (denoted as R2, R3..), particularly the star pattern centred over the Mersey Light Buoy in Liverpool Bay.

Time and Space Wavemill data was analysed over the area near Mersey Bar Light, over which the environmental conditions are assumed constant. Runs R2 to R8 near the Mersey Bar Light all occur within about 1 hour, between 00:18 to 01:27UTC.

Currents These runs occur during maximum ebb (westward) flow. The current measured by the top bin of the ADCP (4m to 2m depth) at Mersey Bar Light and by the 4x4km^2 HF radar indicate that the current flow is stable during the flights. Average (and extreme) values measured by the ADCP are 0.72([0.68,0.77]) m/s flowing to 272° ([267°,275°]), and for the closest HF radar cell, 0.73 ([0.66,0.76]) m/s flowing to 288° ([285°,289°]). In general, the current measured by the HF radar is oriented further North than the ADCP, probably due to wind drift effects linked to the wind coming from the South (see information on wind below).

Waves Directional wave spectra are measured by the directional wave buoy at Mersey Bar Light (Fig 2b). The spectrum shows a weak swell system (in both amplitude

National Oceanography Centre
NATURAL ENVIRONMENT RESEARCH COUNCIL

Figure 1 – Summary of geophysical conditions on the 26th of October, 2011. Blue lines and elongated red strips represent respectively the aircraft flight track and the SAR sampled area. The large coloured arrows summarise the main geophysical conditions at the time when the star pattern data was acquired. The big green square represents the area study in this report with the star pattern.

and wavelength — $H_s = 0.5$m, $\lambda = 70$m) travelling into the area from the North-West (fig. 2b, 2c). The secondary peak in the spectrum is due to the wind and indicates shorter wind waves travelling into the area from 240° ($\lambda \approx 10$m).

Wind Wind speed was observed with the Oceansat-2 scatterometer (12.5km resolution) on the 26th at 00:15 and found closest to the buoy to be around 5–6m/s, in a northward direction (i.e. from the south). In situ wind speed measure close to the coast at Hilbre Island (53.38°N 3.22°W) varies between 4.8 to 5.5m/s northward. The HF-radar provides wave direction measurement of waves around ten meters wavelength which are usually associated with the wind direction (true for a fully-developed sea). In this campaign, there is a limited fetch effect due to the proximity of the coast to the south and the southerly wind, so that these 10m waves are not developed enough to be aligned with the wind. Wave direction indicated by the HF-radar is consistent with the direction of the wind peak in the wave spectrum at about 225°.

Bathymetry Data are acquired in a shallow area (15m to 25m — white square in fig. 2a), meaning that some shoaling of longer swell waves may be present.

National Oceanography Centre
NATURAL ENVIRONMENT RESEARCH COUNCIL

(a)

(b)

(c)
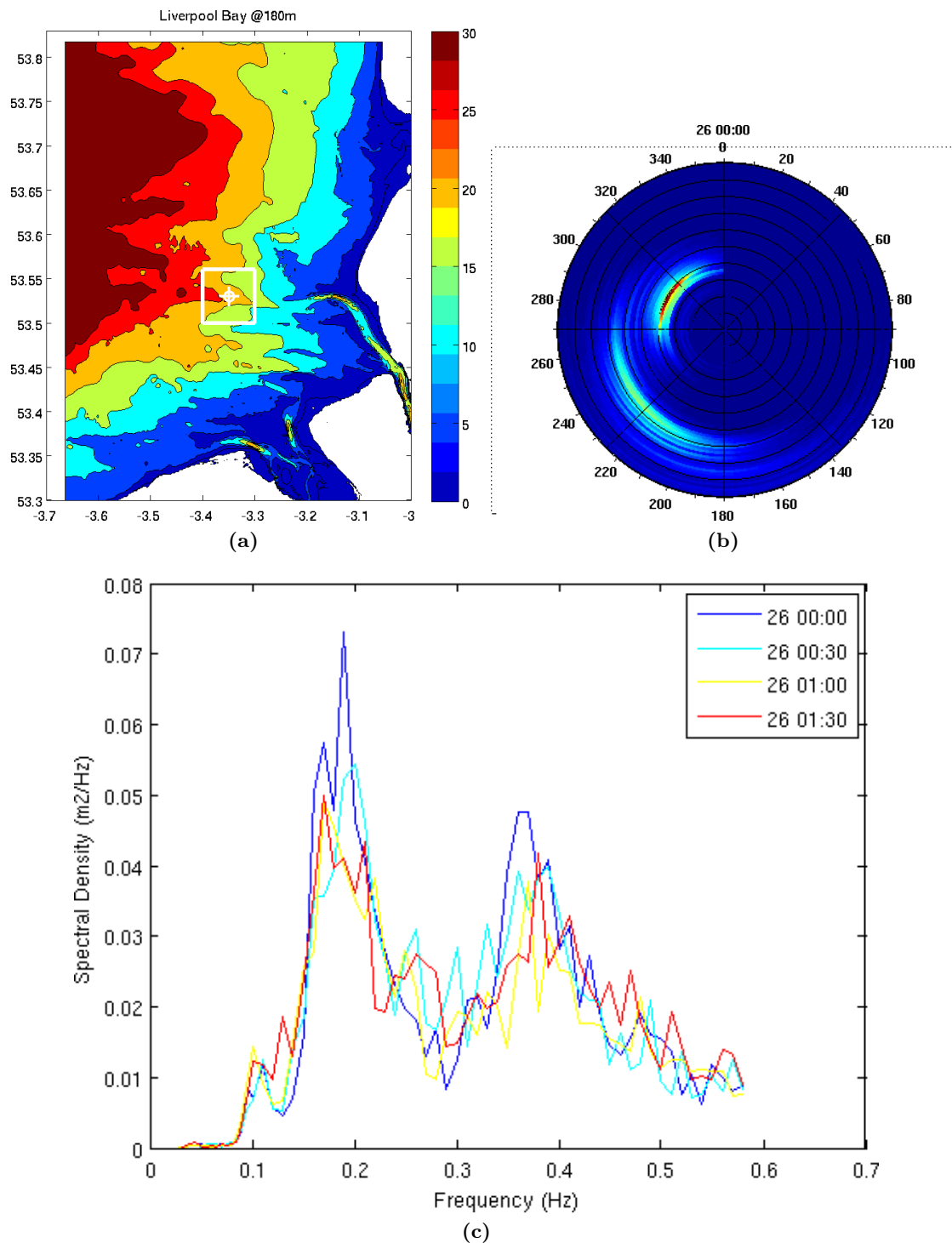
Figure 2 – (a) Bathymetry over Liverpool Bay at a spatial resolution of 180m. Contour lines are plotted every 5m depth. The white cross represents the position of the Mersey Bar Light buoy where the directional wave spectrum is measured and the ADCP is deployed. (b) Wave frequency-direction spectrum on the 26th of October at 00UTC. (c) Wave spectral density every 30min during the airborne site overfly. Wave direction of the peak at around 0.2Hz is 300° and at 0.4Hz is 240°.

Table 1 – Run characteristics, including aircraft mean heading and mean azimuth look direction of the fore and aft antenna

Run	Heading (°)	Mean Fore (°)	Mean Aft (°)	Time (UTC)
2	39.1	351.1	267.1	00:18–00:22
3	180.0	130.9	47.1	00:30–00:34
4	0.0	310.9	227.0	00:39–00:43
5	134.4	85.8	2.0	00:53–00:56
6	289.3	239.5	155.6	01:00–01:04
7	90.0	40.8	316.9	01:16–01:20
8	251.8	201.4	117.6	01:23–01:27

Table 2 – Median and interquartile range (iqr) of aircraft attitude and velocity for each run.

	pitch (^{o})		roll (^{o})		drift (^{o})		horizontal velocity (m/s)	
	median	iqr	median	iqr	median	iqr	median	iqr
R2	1.7	0.7	-0.7	2.7	-3.4	1.2	85	1.0
R3	1.6	0.9	0.3	2.5	-2.4	1.1	70	1.1
R4	1.8	1.1	0.1	2.5	1.4	1.2	85	1.7
R5	1.7	0.8	0.2	2.9	-6.8	1.8	73	1.5
R6	1.5	0.9	0.2	2.1	5.7	1.0	76	0.8
R7	1.3	0.8	0.2	2.1	-6.5	0.7	81	1.3
R8	1.8	0.8	0	1.8	4.9	1.0	70	2.9

2 Wavemill PoC Airborne data

2.1 Aircraft attitude and velocity

Aircraft attitude and velocity for each run on the 26th October star pattern are summarised in table 1 and table 2. Drift angle (difference between heading and velocity direction) and horizontal velocity are relatively different from run to run due to the impact of the wind on the aircraft. Absolute drift angle is up to 7° for runs (R5, R6, R7) which are perpendicular to the wind and horizontal velocity is around 77 m/s ± 8 m/s depending if the run is facing the wind or not. Pitch and roll are on average similar for all runs but the roll variability is higher for some runs (R5, R2) than others (R6, R7, R8).

2.2 SAR system and data

2.2.1 Wavemill SAR system

The Wavemill SAR system is composed of four antennas functioning in X-band and VV-pol. The system is mounted on a gimbal which corrects for the roll and yaw (but not the pitch) of the aircraft. The gimbal should permit to keep a constant roll and yaw angle up to few second arc degree in the range of ± 5° (Sam Doddy pers. comm.).

On 26 oct 2011, the Wavemill system operated in a Javelin configuration with a physical interferometric baseline only in the along-track direction (ATI). The four antennas work in pairs, separated by an ATI baseline of 50 cm along the main axis of the aircraft. Each pair has a squint (yaw) angle in azimuth with the aircraft, with one antenna looking forward (called for simplicity the "fore" antenna) and the other looking backward (called the "aft" antenna). The fixed incidence angle of the antennas is not known, and neither is the beam pattern or beam width. At the sea surface the mean squint angle for each antenna is ±45°. Each pair is composed of a master and a slave antenna. Only the master emits, both antennas receive. The effective baseline is then half of what it would be if both the master and slave antenna were emitting (cf [Carande, 1994]).

2.2.2 Available Wavemill SAR data

The Wavemill SAR data was provided to NOC by Starlab. The coverage and location of the Wavemill SAR data available to NOC are represented in Figure 3. Only about one third of the acquired Wavemill data represented in Figure 1 were distributed to NOC for reasons which are not clear. All the available data (except R3) are located over the Mersey Bar Light (MBL) where the in situ sea surface current and wave are measured.

The SAR data field used in this report are:

- Amplitude of single look images from the master or slave antenna (no sigma0, no calibration) at high resolution;

- Interferogram (or interferometric phase) at high resolution;

- Surface current computed by Starlab at a spatial resolution of about 100 m.

The spatial resolution of the high-resolution products varies across track from 1m at far range to 5m at near range. Along track resolution is 5m.

In the Javelin configuration, the squint angle at the surface changes with range. At near range, the squint angle is ±65° for the fore or aft antenna at near range, ±45° at mid range and ±32° at far range (computed by Starlab).

3 Surface Current Retrieval Model

SAR along track interferometry (ATI) permits the measurement of surface velocity (U_{surf}), defined as the line-of-sight velocity (U_{los}) projected on the mean sea surface. The ATI SAR actually measures the surface Doppler velocity, which is the power-weighted sum of the line-of-sight velocities within the resolution cell of the radar. It has been shown that the Doppler velocity comprises both ocean currents (including wind drift and Stokes drift) and other unwanted surface motions, particularly associated with wind (Bragg scatterers) and waves (orbital velocity), the latter being a particularly dominant influence.

In the next section, the relation between SAR ATI interferogram and the derived line-of-sight or surface velocity is presented, followed in Section 3.2 by the description of a simple theoretical model to compute the wave-induced artefact surface velocity.
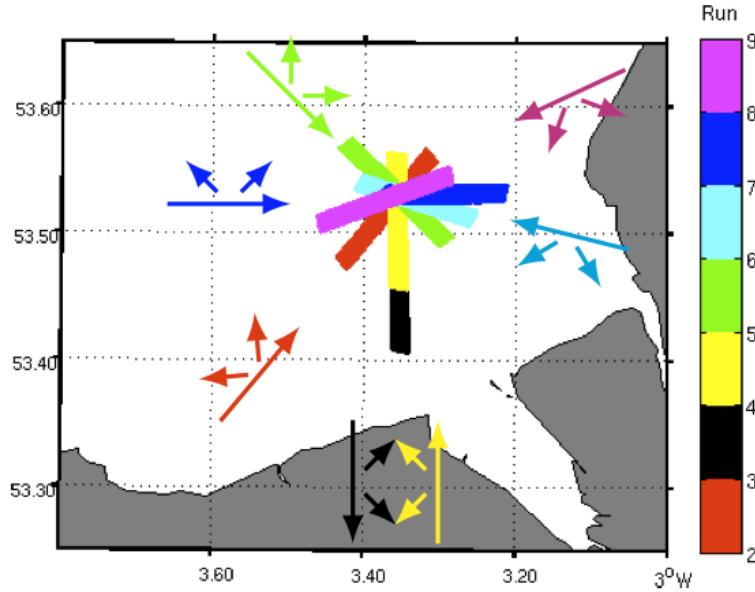
Figure 3 – Airborne data available near the Mersey Bar Light for the 26th of October. Each runs are represent with a different color. The color large arrow represents the aircraft flight direction for each run and the two small arrows represent the line-of-sight direction of the fore and aft antennae.

3.1 Retrieving line-of-sight and surface velocity from SAR ATI

SAR ATI relies on the same area being imaged with a very short time lag (τ). This time lag τ has to be short enough to ensure coherence of the signal is preserved between the two images. In practice, the time lag is related mainly to the distance (D) between the two antennas and the velocity of the aircraft (V), but also to the pitch and drift angle of the aircraft. When only the master antenna emits, the interferometric baseline is halved [Carande, 1994] and we have:

$$\tau = \frac{D_{eff}}{2V} \approx 3ms, \qquad \text{and} \tag{1}$$

$$D_{eff} = \frac{D}{\cos(\text{pitch})\cos(\text{drift})}. \tag{2}$$

The autocorrelation function of the backscattered field is related to the Doppler spectrum via the Fourier transform. The autocorrelation function ($R(\tau)$) of the backscatter from each pixel at lag time τ is:

$$R(\tau) = E\left\{B(t).B^*(t-\tau)\right\}, \tag{3}$$

where E denotes ensemble averaging and $B(t)$ is the complex backscattered field from a particular pixel at time t.

The pixel-by-pixel phase difference between the two complex SAR images is called the interferogram, and is equal to the argument (phase) of $R(\tau)$. Under the approximation

11

$\omega\tau << 1$, the interferogram ($\Delta\phi$) is then simply related to the mean Doppler frequency ($\overline{\omega}$) [Thompson and Jensen, 1993, Graber et al., 1996] through:

$$\Delta\phi = \arg\{R(\tau)\}$$
$$\approx \overline{\omega}.\tau \qquad (4)$$

According to [Graber et al., 1996] the error introduced by the approximation is less than about 10%.

This gives then the line-of-sight velocity:

$$U_{los} = \frac{\overline{\omega}}{2k_e} \qquad (5)$$
$$= \Delta\phi\frac{\lambda_e V}{2\pi B_{eff}}$$
$$\approx 0.7\Delta\phi$$

and then the surface velocity:

$$U_{surf} = \frac{U_{los}}{\sin\theta}. \qquad (6)$$

3.2 A simple model to compute Doppler frequency wave artefact velocity

The model described here is taken from [Chapron et al., 2005]. The model represents the correlation between the tilt modulation of the backscatter amplitude and the wave orbital velocity as illustrated in Figure 4.

The wave artefact contribution is modelled as:

$$T(\varphi) = \frac{1}{\tan\theta}\frac{1}{\sigma_0}\frac{\partial\sigma_0}{\partial\theta}\int k\omega S(\vec{k})d\vec{k} \qquad (7)$$

where φ is the azimuthal direction, σ_0 the normalized radar cross-section (NRCS), k the ocean wave wavenumber, and S the directional elevation wave spectrum. $S(\vec{k})$ is computed as $S(\varphi, k) - S(\varphi - \pi, k)$ and represents the contribution of the wave motion in the line-of-sight direction. It takes into account the contribution from waves propagating away and toward the radar. If only one component is used, the behavior of the model is not consistent with the observations.

As a large range of ocean length scales are considered, it is more convenient to represent the wavenumber in logarithmic scale. To simplify the interpretation of the contribution to the integral, the integration variable is changed from k to $\log k$:

$$T(\varphi) = \ln 10\frac{1}{\tan\theta}\frac{1}{\sigma_0}\frac{\partial\sigma_0}{\partial\theta}\int k\omega S(\vec{k}).k.d(\log\vec{k}) \qquad (8)$$

The model is based on the Geometrical Optics approximation, so the integration of the spectrum should be limited to wavenumbers lower than one third (1/3) or one fifth (1/5) of the electromagnetic wavenumber i.e ($k_{cut-off} = k_e/3 \approx 70$ rad/m). In this
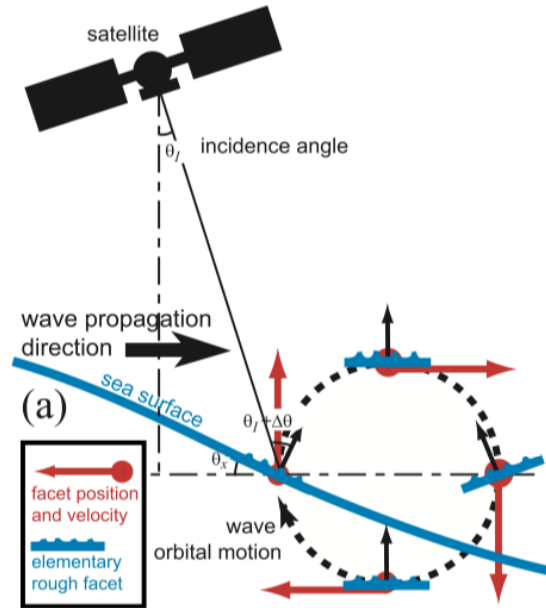
Figure 4 – Schematic of the conceptual model of the measurement of surface velocity and the contribution of radar cross-section modulation by waves from [Chapron et al., 2005].

implementation of the model, the tail was not removed but this does not change the behavior of the model more than 0.05 m/s.

The model depends on two main terms: the gain factor G (see below) and the content of the integral. [Chapron et al., 2005] introduces the gain factor $(G(\theta))$ as:

$$G(\theta, \varphi, u_{10}, \lambda_e) = -\frac{1}{\sigma_0}\frac{\partial\sigma_0}{\partial\theta} \tag{9}$$

which depends on the incidence angle (θ), relative azimuth to wind direction (φ), wind speed (u_{10}) and electromagnetic wavelength.

To compute this gain factor for the Wavemill PoC data, as there is no geophysical model function (GMF) for the NRCS in X-band, we apply a proportionality factor between a C-band and Ku-band GMF from CMOD5 and NSCAT1 respectively. The estimated gain factor (fig. 5) decreases when wind speed increases, as the NRCS slope with incidence angle is less steep at higher winds and decreases with incidence angle. There is also small variation ($\pm 10\%$) with azimuth angle to the wind: higher absolute values of the gain factor are seen crosswind rather than upwind, as the steepness of the NRCS slope with incidence angle is larger in the crosswind direction. The values of the gain factor obtained are consistent with the values reported in [Chapron et al., 2005].

The content of the integral in Equation 8 provides insight into the sensitivity of the wave-induced velocity to various parts of the wave spectrum. Figure 6 presents the sensitivity of the wave orbital velocity to wavenumber for (left) a KHCC wave spectrum [Kudryavtsev et al., 2003] generated for fetch limited conditions ($\Omega = 1.4$) and a wind of 5.5 m/s from 200° (fig. 6a) and (right) for the wave spectrum measured by the buoy
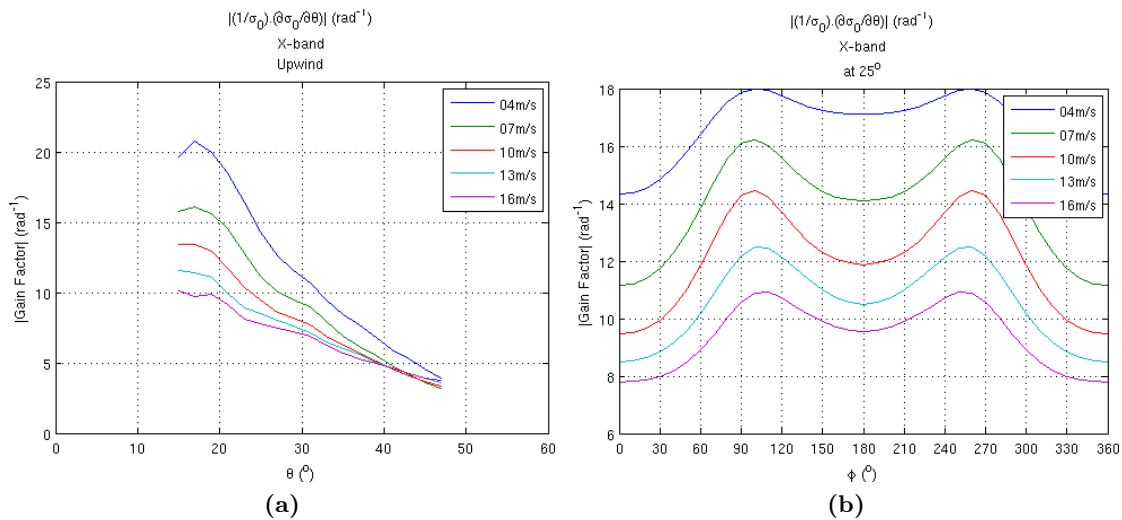
Figure 5 – X-band gain factor for various wind speed as a function of (a) incidence angle for upwind, (b) azimuth for an incidence angle of 25° with 0°, 90°, 180° corresponding respectively to up/cross/down-wind.

at Mersey Bar Light, which has been extended to short wavelengths using the tail of the KHCC wave spectrum (fig. 6b). The different colours indicate different azimuth directions with respect to wind direction. The sensitivity is maximum around a wavenumber of 1 rad/m i.e. wavelength of 6 m. There is perfect upwind, downwind symmetry (same magnitude, different signs).

The wave artefact surface velocity is the product of the gain factor and the wave orbital velocity integral and is shown in Figure 7. The wave artefact velocity decreases rapidly with incidence angle in the range 15–30° and decrease more slowly for higher incidence angle (fig. 7a). The upwind/downwind asymmetry[1](fig. 7b) is due only to the gain factor asymmetry. The gain factor magnitude is higher for downwind than upwind. This asymmetry is opposite to the satellite observation [Mouche et al., 2012] (Envisat ASAR) and from our airborne observations (see below).

4   Surface current retrieval results

In the first section, the analyses focus on the available runs in the star pattern near Mersey Bar Light. Geophysical conditions are assumed uniform in space (about 10km) and in time (about 1 hour), and the variability in the SAR measurements and the aircraft attitude and velocity within each run is assumed negligible . In the second section, the variability within each run is briefly explored, to confirm the presumed origin of some of

---

[1]There was an error in the results presented at the PM3 meeting at Barcelona in May 2014. The up/downwind asymmetry of the previous results was in better agreement with observations but was not consistent with (our understanding of) the simple model described above.
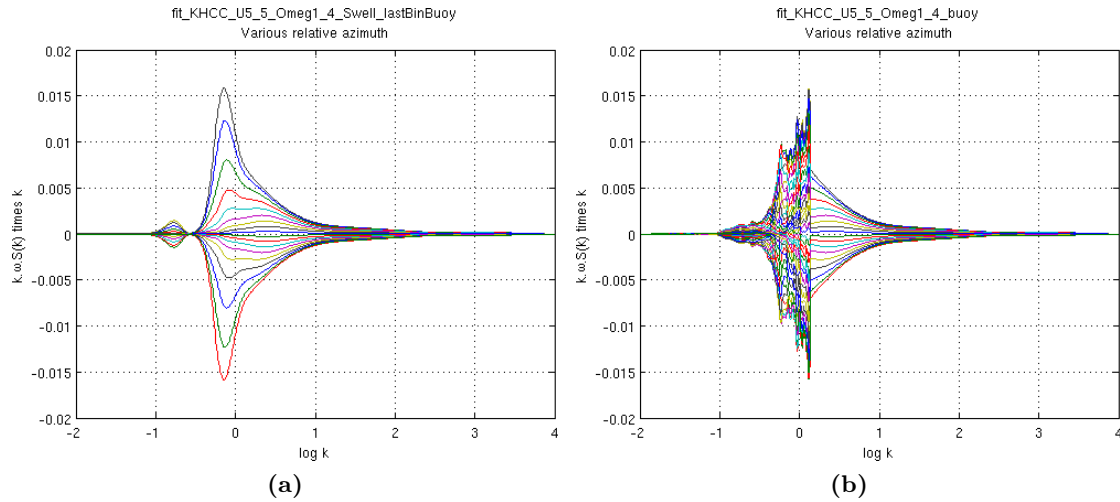
Figure 6 – Wave orbital component in Equation 8 as a function of wavenumber for every 10° of azimuth angle for (a) KHCC model — $U_{10} = 5.5$ m/s, $\varphi = 200°$, $\Omega = 1.4$; (b) buoy measured wave spectrum extended with KHCC for waves with $\lambda < 5$ m.
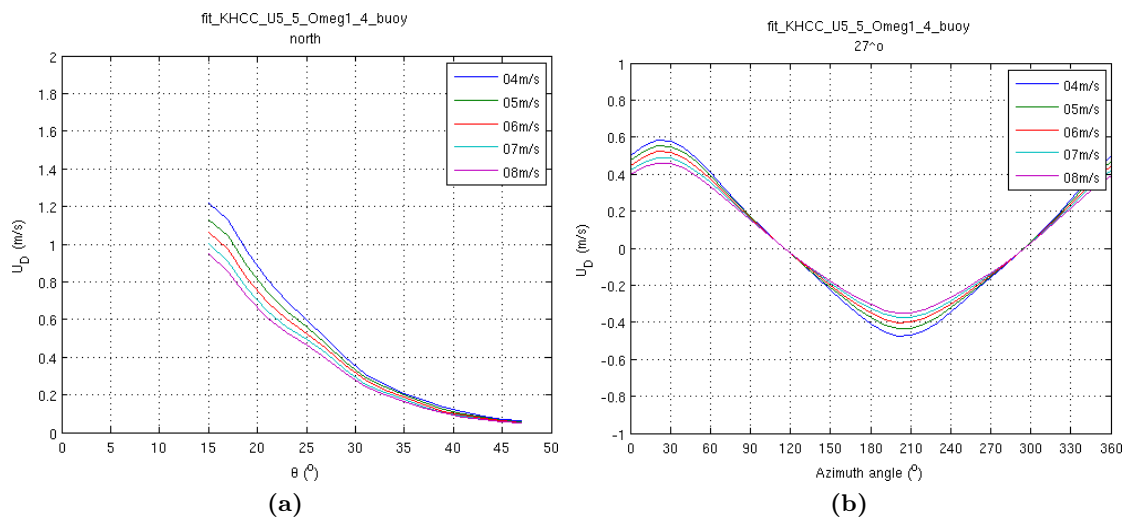
Figure 7 – Wave artefact surface velocity computed with [Chapron et al., 2005] model for various wind speeds as a function of (a) incidence angle for 0° azimuth direction (20° to downwind) and (b) azimuth angle for an incidence angle of 27°. The computation uses the buoy wave spectrum extended with a KHCC spectrum for small waves ($\lambda < 5$ m) .

the results .

4.1 Inter-run Analysis of star-pattern data

All data analysed in this section correspond to the median value taken along the full track of the available run portion presented in Figure 3.

4.1.1 Analysis of SLC amplitudes

Figure 8 shows that the amplitudes of the SLC from the fore and aft antenna are not in good agreement, as for same azimuthal direction with respect to North (color), the amplitudes are different. Despite this, the strongest backscattter signal corresponds to an azimuth direction of about 200° which is close to the upwind direction according to auxiliary information about local wind conditions at the time of the flight.

To determine more accurately the wind direction dependence in this dataset, a second order harmonic curve is fitted to the variation of the amplitude with azimuth direction for each antenna and every 5° in incidence angle (±0.1°) between 25 to 40° (Figure 9). The maximum of the curve (parameter f in the titles of subplots shown in Figure 9) is found between 186° and 204° for all antennas and incidence angles, in agreement with the expected wind direction. The amplitude of the harmonic variation (parameter a for the omnidirectional component) is quite different between the fore and aft antenna with difference of the order of 20%. The amplitude of the first harmonic (parameter b) is similar for the aft and fore antenna for all incidence angles, except at 25° where it differs by about 10%. The amplitude of the second harmonic (parameter c) is about two times higher for the fore antenna than for the aft whatever the incidence angle. This could be due to the wind direction sampling which is different for each antenna or to a sharper beam pattern in 'azimuth' direction for the fore antenna.

To get round the calibration issue of the two antenna, the amplitude observed for each antenna was normalised by dividing by the omni-directionnal component "a" calculated every 5°, then combined (plot not shown) but it does not improve anything.

4.1.2 Analyses of interferograms

Figure 10a shows the median interferogram for each run against (left) incidence angle and (right) azimuth look direction. The interferograms present generally a high dynamic range within and between runs. The median signals present for all runs some noise and a step in the near range (incidence angle less than 26.3°) and higher noise and a step at far range (incidence angle greater than 44°). In the following analyses, all data outside the range 26.3—44° are removed.

The high dynamic range with incidence angle in Figure 10a is mainly related to the azimuth variation of the interferogram seen in fig. 10b, since surface squint angle and incidence angle are correlated. The azimuth variation seems to be dominated by the wind as the maxima are close to the upwind/downwind (South/North) direction. A deeper geophysical interpretation of these results follows later. Note that the measurements
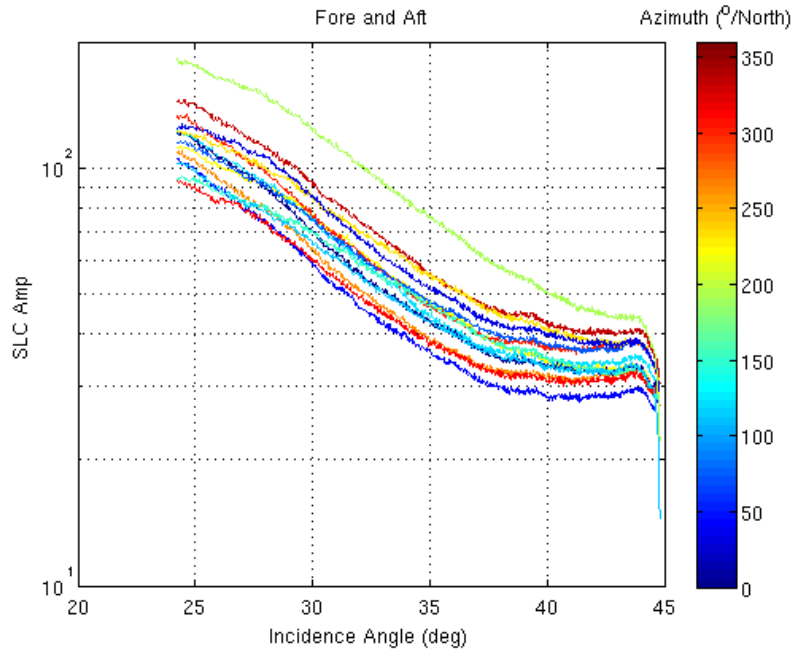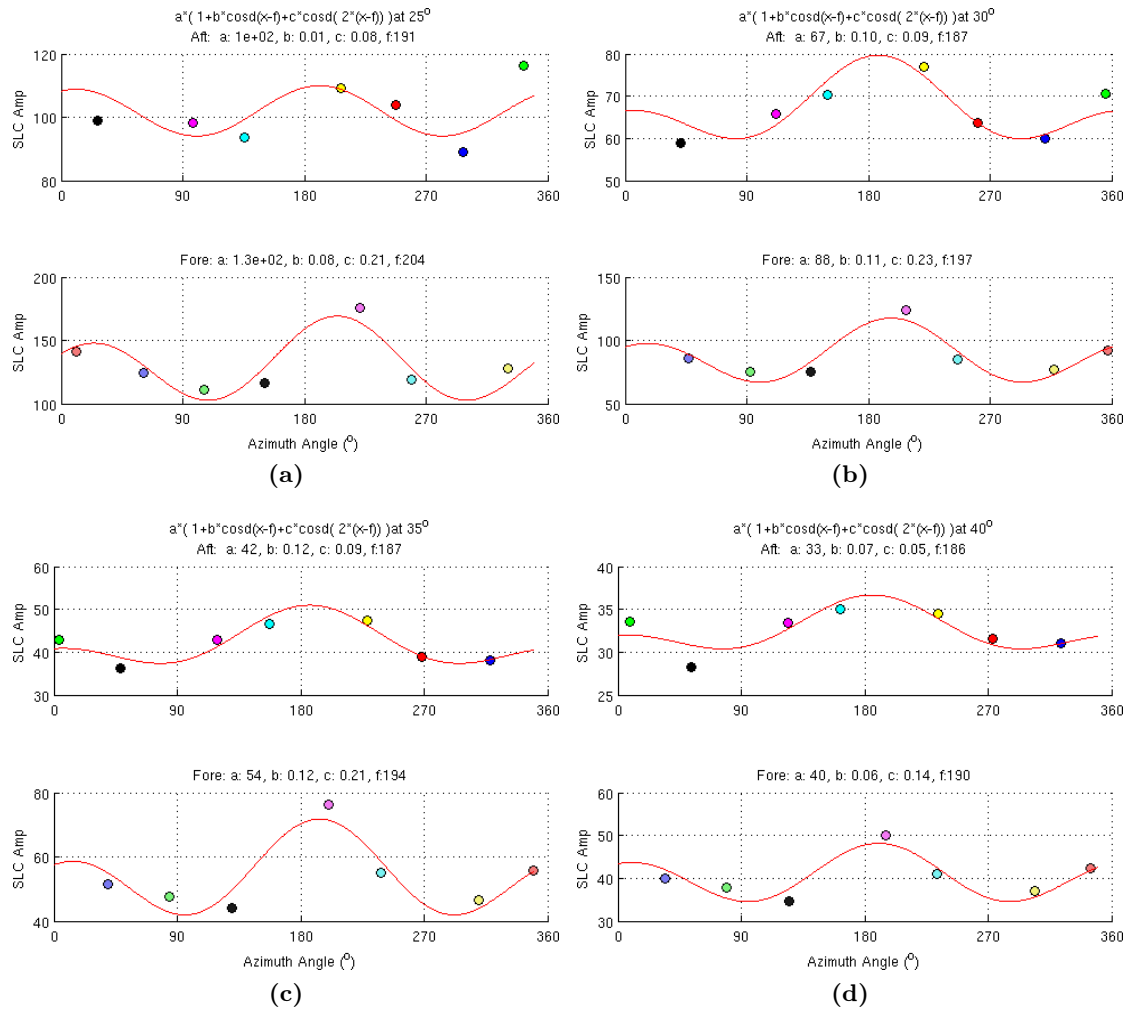
Figure 8 – Median amplitude along track for each run as a function of incidence angle. Colour represents the azimuth look direction of the aft or fore antenna with respect to the North following oceanographic convention. Amplitude is shown on a logarithmic scale.

of the aft antenna in Figure 10b are distinguishable from those of the fore antenna by the use of a brighter colour code and because the circle markers are located left of the triangles. The dynamic range of the interferograms is quite different for the aft and fore antenna, being higher for the aft and flatter with incidence angle for the fore.

4.1.3   Analysis of line-of-sight velocities

For easier geophysical interpretation, the interferograms are converted to apparent line-of-sight velocity (U_{los}) or to the horizontal apparent velocity (U_{surf}) according to Equation (5) and 6. The line-of-sight velocity (Figure 11a) is roughly proportional to the interferogram , within about $\pm 10\%$. This $\pm 10\%$ is mainly due to aircraft velocity variations between runs (Table 2) depending if the flight path is oriented upwind or downwind. This proportionality coefficient is largest for runs R2 and R4 and smallest for runs R3 and R8 (see Table 2).

The azimuth variation of the surface velocity (Figure 11b) presents the same general behaviour with azimuth as the line-of-sight velocity (Fig 11a) and the interferogram (Fig 10b) but with some large dynamic differences for runs with the highest absolute amplitude.. The extrema occur around 180° and 330° and do not align either with the direction of the wave-induced artefact current (around 200°; see fig. 7b), nor with the ADCP measured current. If the ADCP measured current component is removed from the measured surface velocity at each azimuth direction (fig. 12), there should remain

Figure 9 – Median amplitude along track versus azimuth look direction of the antenna for incidence angle of (a) 25°, (b) 30°, (c) 35°, (d) 40°. Top (resp. bottom) panels are for the aft (resp. fore) antenna. Colour of each point refers to the same colour code as for Figure 3. The expression of the fitted second harmonic curve and the coefficient of the fitted curve are indicated in the title of each panel.

National Oceanography Centre
NATURAL ENVIRONMENT RESEARCH COUNCIL
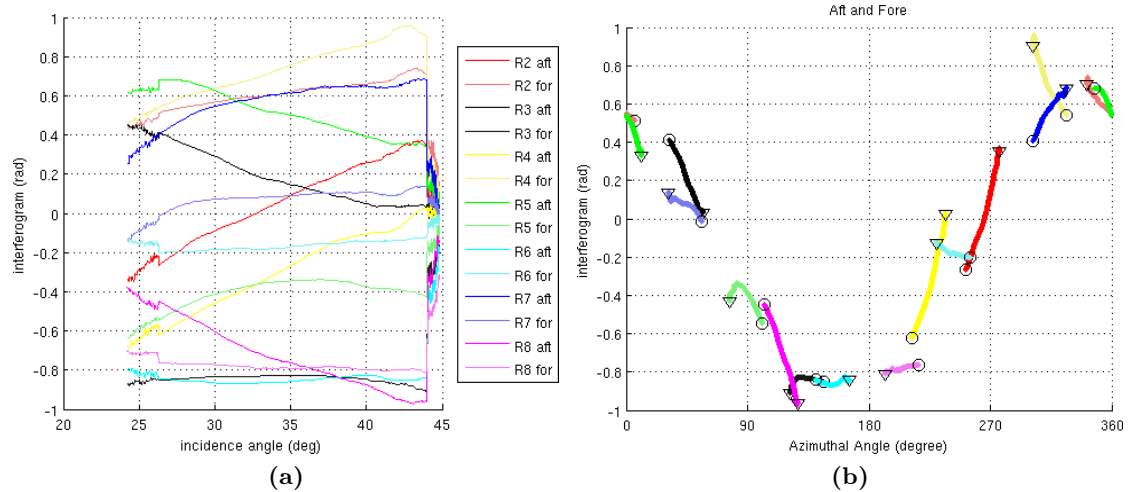
Figure 10 – Median interferogram for each run as a function of (a) incidence angle for all azimuth directions (b) azimuth look angle for all incidence angles. Colour code of each run is the same as in Figure 9 and is represented in the legend of (a). The circle (triangle) represent the near (far) range for each run.

only the wave-induced artefact current component. Indeed what is observed shows very good agreement in phase with the wave-induced current predicted by the Chapron et al. 2005 model (fig. 7b). The amplitude of the model is about 0.5 m/s at 27° much lower than the observed ones at 26.3° (around 1 m/s).

The results also indicate, as expected, a lower amplitude of the wave-induced artefact current amplitude at far range (high incidence angles) than at near range (fig. 12b and c).
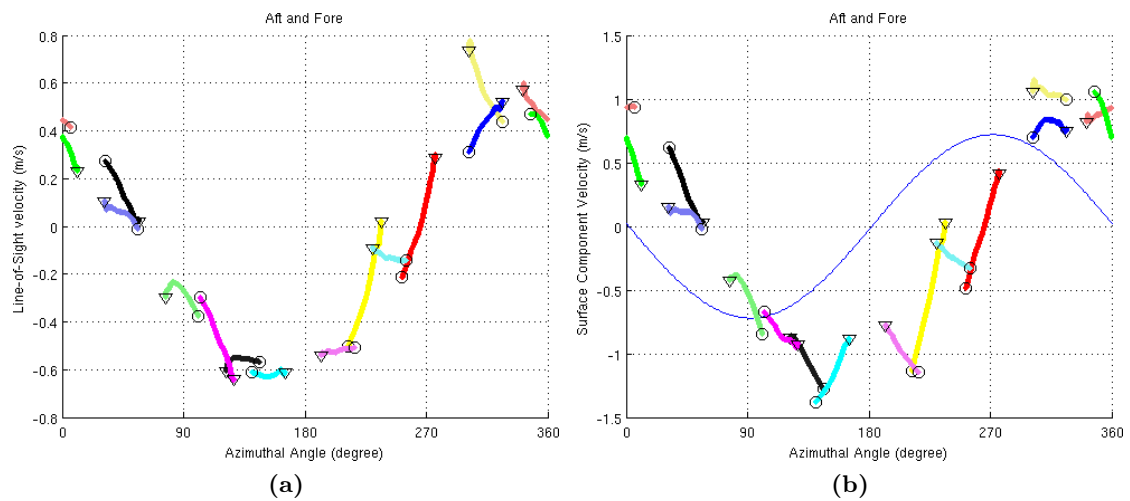
Figure 11 – Median (a) line-of-sight (b) surface velocity as a function of azimuth angle for each run. Same colour code and legend as in Section 4.1.2. In (b), the blue curve represents the projected component of the sea surface current (as measured by the ADCP) for every azimuth angle.

(a)

(b)

(c)
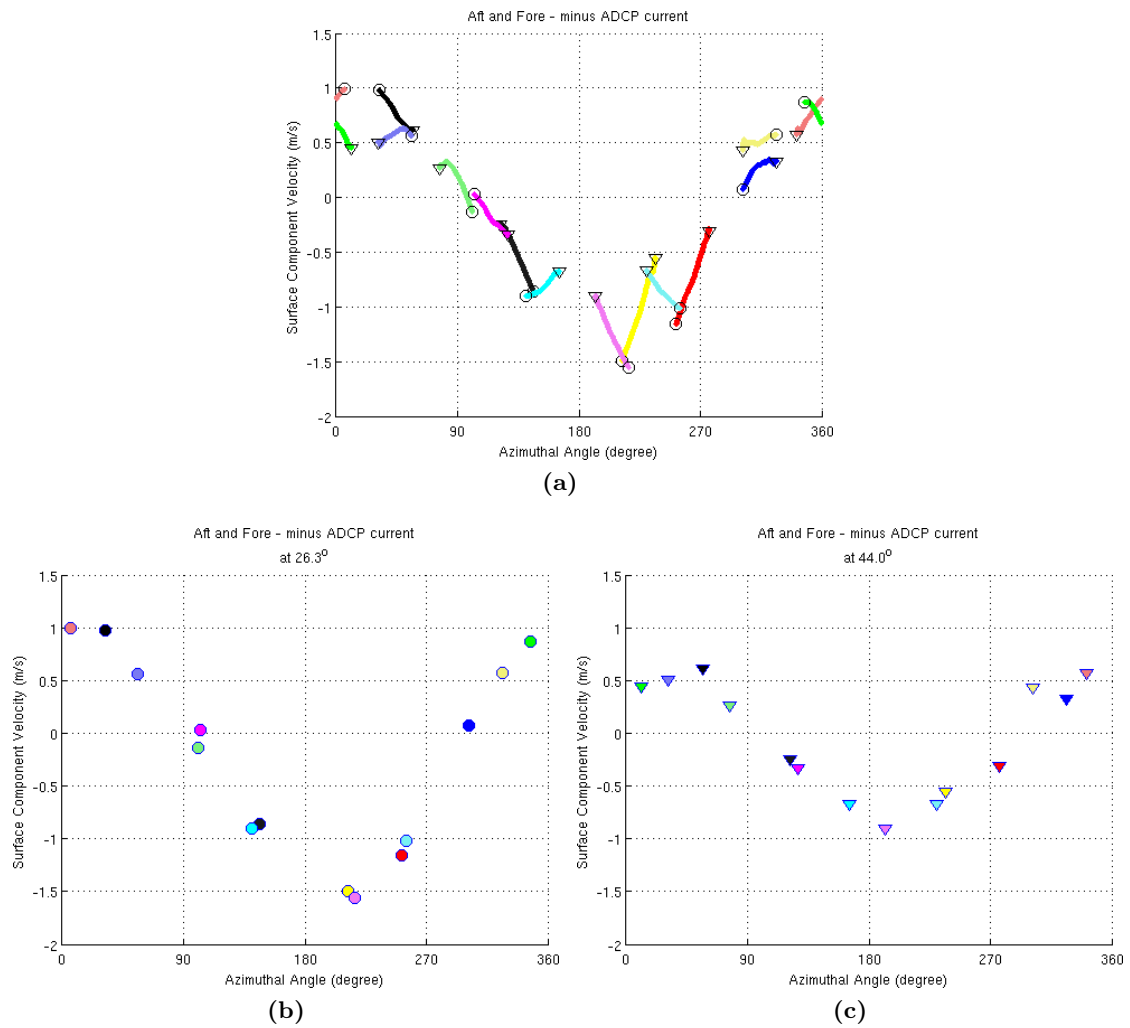
Figure 12 – (a) Median residual current (computed as measured surface velocity minus ADCP current) for each run against azimuth angle. (b) same as (a) but for the near range only. (c) same as (a) but for far range only. Same colour code as in Section 4.1.2.
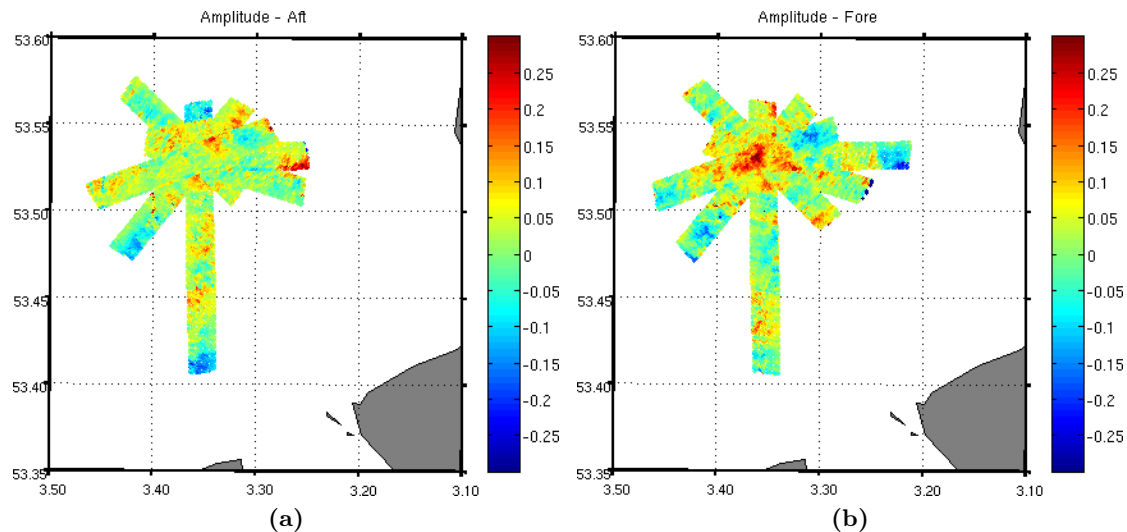
Figure 13 – SAR amplitude after removing the median incidence angle amplitude dependence for each run and averaging to 100m.

4.2 Intra-run variability

4.2.1 SLC Amplitude

There is some strong variability in the amplitude of the SLC for all runs, but none of the observed signatures can be attribute to any obvious features in the area or to any particular geophysical effect (fig. 13).
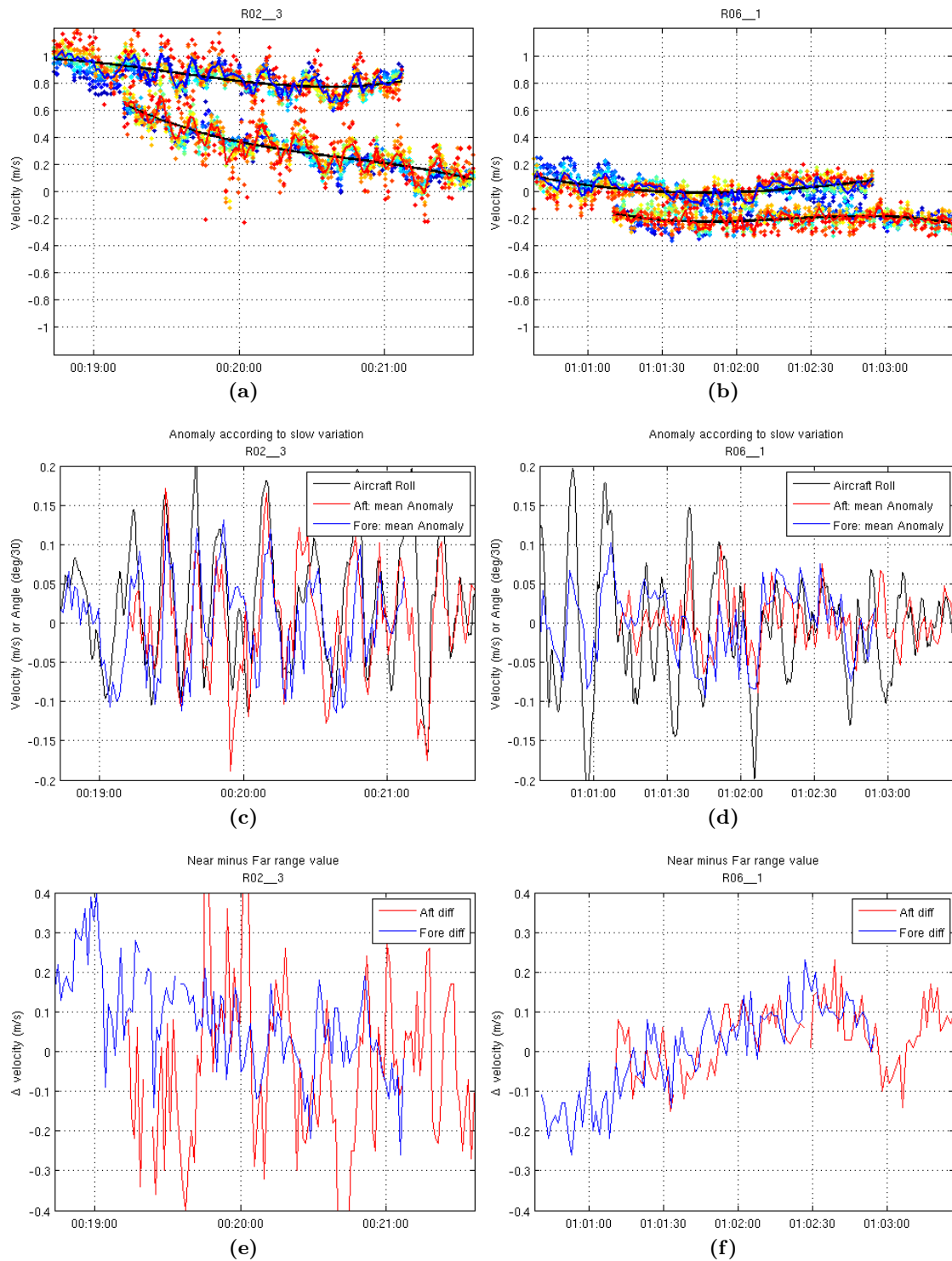
4.2.2 Retrieved surface velocity

In this section, the velocity data produced by Starlab were compared with the aircraft attitude (obtained from ADS). Unfortunately, the same exercise cannot be repeated with the interferogram dataset as there is no time stamp field in provide by Starlab.

Two questions arise as a result of these intra-run analyses. 1) Is the median value representative of the whole run portion? 2) How big is the intra-run velocity variability?

The first question relates to the variation in geophysical conditions over about 10km (or 2 minutes of flight). Except for Run 2 (fig. 14a), there is no long trend larger than the noise (0.2 m/s). For Run 2, the fore antenna (pointing close to north — 351°) the velocity changes by about 0.6 m/s along the run. This could be due to increased sensitivity to wave artefacts as the fetch increases further north, away from the coast.

The second question is related to variations over much shorter time scales which could be due either to local sea surface effect, or to attitude motion of the aircraft. The Starlab surface velocity field are averaged at about 100 m resolution. The impact of local sea surface effect is not investigated, but focus instead on the aircraft attitude effect.

Figure 14 – (top) Starlab-derived surface velocity for the fore and aft antenna for runs R2 and R6 as a function of distance (or time) along track. Cold dots correspond to near range, warm dots to far range. The blue and red curves represent the average surface velocity retrieved with the aft and the fore antennae. The black curve represents the long time trend through the run.
(middle) Black curve: aircraft roll; Blue and red curves: anomaly of retrieved surface velocity (blue and red curve in upper panels) against the long time trend.
(bottom) Red curve: near range minus far range velocities along track for aft antenna; Blue curve: opposite for the fore antenna (far range minus near range).

First, the large trend along-track is removed, which is possibly linked to large scale changes in geophysical conditions in the run, and the anomaly from this trend is examined (fig. 14-middle panel). When the across-track averaged anomaly is highly correlated between the fore and aft antenna, it is also correlated with the roll angle of the aircraft. From this, the influence is of the order of about 0.03 m/s per degree of roll angle of the aircraft.

To emphasise the oscillations around the mean of the near-range (cold colour) and far-range (warm colour) retrieved velocity (fig. 14b), the difference between the far-range and near range velocities is computed for each antenna (fig. 14-bottom panel). Some variations seem to be highly related, with a stronger link for R6 than for R2 or any other. This seems to suggest a link with the aircraft drift angle variation around the mean drift angle during the run (not shown).

Surprisingly, it emerged that the aircraft attitude motion (roll and yaw) were corrected with a gimbal which should correct the roll and yaw of the aircraft with an accuracy of one sec degree (pers. comm. with Sam Doddy) in the range $\pm 5°$. No inertial unit was fixed on the antenna. The accuracy of the attitude correction can therefore not be confirmed.

In summary, the aircraft attitude motions seems to have a significant impact on the Starlab-derived surface velocity, but it is not possible to conclude whether thisis due to the interferometric SAR processing or to residual errors caused by the attitude motions from the aircraft or the gimbal. Figure 15 show the variation in azimuth of the Starlab-derived velocity, using the same colour codes, ancillary data and conventions as those in Figure 11b and Figure 12a. It is not clear what is the origin of the discrepancy between the surface velocity derived by NOC from the interferograms and the Starlab-derived surface velocities.

4.3 Preliminary analysis of Wavemill hybrid configuration on 27 Oct 2011

A quick analysis of the Wavemill data obtained with the hybrid configuration on 27/10/2011 was attempted but several issues made it impossible to continue:

- The interferogram phase reports values between -2 and -15 for the aft antenna and between 2 and 15 for the fore antenna (fig. 15b, c and d). These values seem close to 4π but should they not be within $[0, 2\pi]$ instead? Are these values in radians?

- It seems there is some interferogram phase wrapping (very explicit and extreme in fig. 15c) but these wrapping never occur at a constant phase.

- The amplitude of the SLC presents very strange characteristics with amplitudes from different runs crossing along incidence angle (fig. 15a). If the results are plotted as function of azimuth angle, no sinusoidal variation of the amplitude is found with azimuth.
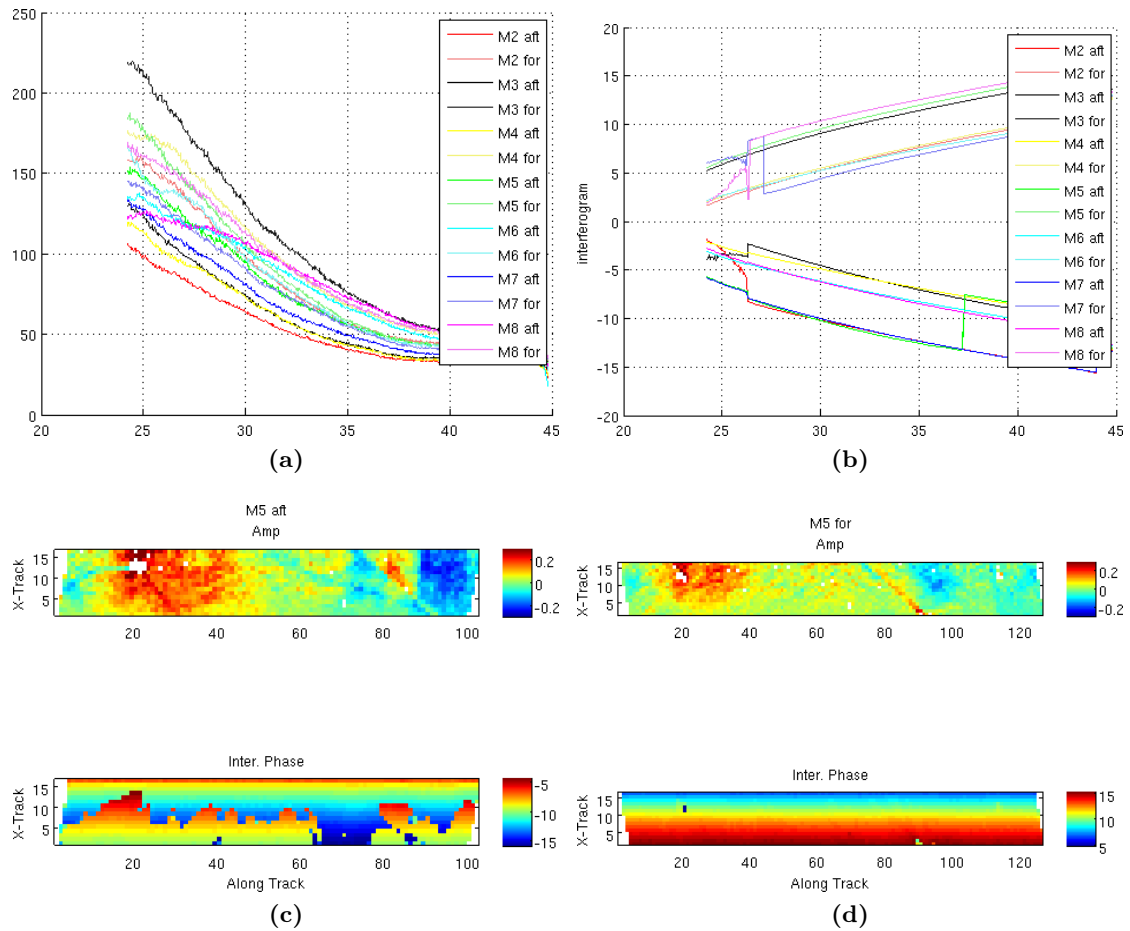
Figure 15 – SAR airborne data for the 27th of October 2011 in the Hybrid configuration (ATI + XTI baseline). (a) Median amplitude for each run as a function of incidence angle. (b) Median interferogram phase as a function of incidence angle. (c resp. d) 100m averaged map of (top) normalised amplitude and (bottom) interferogram phase for run M5 aft (resp. fore) antenna.
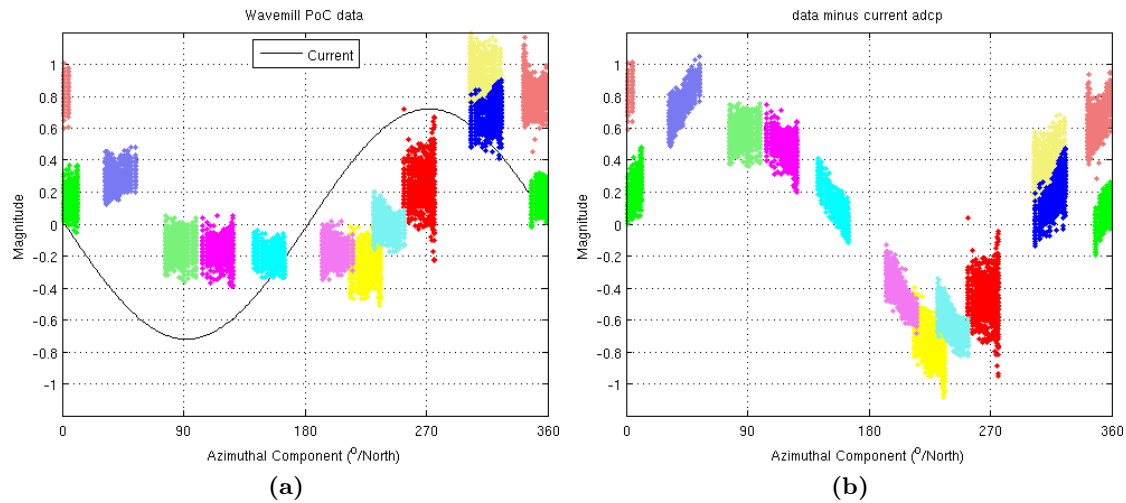
Figure 16 – (a) Surface velocity derived by Starlab (in m/s) for each run as a function of azimuth direction. The black curve represents the component of the sea surface current (ADCP). (b) Surface velocity minus sea surface current. Colour code is the same as for Figure 11b.

5   Outstanding questions & comments

- There is discrepancies between the surface velocity derived in this work from Equation (6) (fig. 11b) and those derived and provided by 'Starlab' (fig. 16a). The surface velocity residual (measured minus ADCP current) (fig. 12a and 16b) should correspond to the wave-induced artefact surface velocity. The wave artefact current derived in this work from Equation (6) shows better agreement with the estimates from the Chapron et al (2005) model in the phasing in azimuth, but not in amplitude (fig. 7). What are the differences in the surface velocity computations between what is present here and the approach used by Starlab?

- The wave artefact model is in very good agreement in phase with the airborne observations, but the upwind/downwind asymmetry and the magnitude of the current are not well captured by the model. The model upwind/downwind asymmetry is opposite to what is observed both in airborne data (fig. 12) and EnviSAT ASAR satellite data [Mouche et al., 2012]. This opposite asymmetry originates from the gain factor, where the gain factor was derived from a satellite-derived GMF (CMOD5 and NSCAT GMF). The amplitude of the wave artefact current estimated by the model ($\approx$0.5 m/s at 27° and $\approx$0.1 m/s at 44°) is much smaller than the current derived from the airborne observations ($\approx$1 m/s at 27° and $\approx$0.5 m/s at 44°) and those reported for Envisat ASAR [Mouche et al., 2012].

- Aircraft roll and drift angles have significant impact on the derived velocity, even though the antenna should not feel these attitude motions because of the use of a gimbal. There is no significant relation between the SLC amplitude and the roll or

26

drift angles. What possible explanation is there for this?

- Only approximately one third of the data acquired in the star pattern runs over the Mersey Light bar have been provided (see difference in coverage and extent of the runs in fig. 1 and fig. 3). Is the whole dataset of every run in the star pattern processed and/or available?

In order to publish these data in a peer-review article, it would be desirable to perform an analysis of the coherence of each run and to conduct of proper analysis of the aircraft attitude influence on the phase 'noise'. For this, it would be necessary to have for each run and each fore or aft system antennas:

- Complex images (amplitude and phase) for both master and slave antennas at the same (high) resolution as provided for these analyses;

- Time stamp for every cell as provided for the velocity field;

- Doppler spectrum (if available?). The latter may not be essential for the the paper, but would be useful information if available .

References

[Carande, 1994] Carande, R. (1994). Estimating ocean coherence time using dual-baseline interferometric synthetic aperture radar. *Geoscience and Remote Sensing, IEEE Transactions on*, 32(4):846–854.

[Chapron et al., 2005] Chapron, B., Collard, F., and Ardhuin, F. (2005). Direct measurements of ocean surface velocity from space: Interpretation and validation. *Journal of Geophysical Research: Oceans*, 110(C7):n/a–n/a.

[Graber et al., 1996] Graber, H. C., Thompson, D. R., and Carande, R. E. (1996). Ocean surface features and currents measured with synthetic aperture radar interferometry and hf radar. *Journal of Geophysical Research: Oceans*, 101(C11):25813–25832.

[Kudryavtsev et al., 2003] Kudryavtsev, V., Hauser, D., Caudal, G., and Chapron, B. (2003). A semiempirical model of the normalized radar cross section of the sea surface, 2. radar modulation transfer function. *Journal of Geophysical Research: Oceans*, 108(C3):FET 3–1–FET 3–16.

[Mouche et al., 2012] Mouche, A., Collard, F., Chapron, B., Dagestad, K., Guitton, G., Johannessen, J., Kerbaol, V., and Hansen, M. (2012). On the use of doppler shift for sea surface wind retrieval from sar. *Geoscience and Remote Sensing, IEEE Transactions on*, 50(7):2901–2909.

[Thompson and Jensen, 1993] Thompson, D. R. and Jensen, J. R. (1993). Synthetic aperture radar interferometry applied to ship-generated internal waves in the 1989 loch linnhe experiment. *Journal of Geophysical Research: Oceans*, 98(C6):10259–10269.

[Wavemill PoC, 2012] Wavemill PoC (2012). *Wavemill Proof-of-Concept Final report: A proof-of-concept airborne campaign using an existing X-band interferometric SAR instrument*. ESA/ESTEC Contract No. 4000103580/11/NL/CT.